

Crustal and Uppermost Mantle Shear Velocity Structure Adjacent to the Juan de Fuca Ridge from Ambient Seismic Noise

Ye Tian, Weisen Shen, and Michael H. Ritzwoller

Center for Imaging the Earth's Interior, Department of Physics, University of Colorado at Boulder, Boulder, CO 80309, USA (Ye.Tian@colorado.edu)

Key Points

Rayleigh wave velocities from ambient noise vary with crustal age near the Juan de Fuca ridge.

Mantle V_s increases with crustal age faster than expected due to conductive cooling alone.

A low velocity zone centered near 20 km depth near the ridge may imply about 1% partial melt.

Abstract

Seismic ambient noise recorded by six months of OBS data from the Cascadia Initiative experiment near the Juan de Fuca Ridge produces Rayleigh wave group and phase speeds from 6-20 sec period. These observations are fit with an age-dependent formula, which we invert using a Bayesian Monte Carlo method for an age-dependent shear velocity (V_s) model to a depth of 80 km between ages of 0.5 Ma and 3.5 Ma. Igneous crustal structure is age-invariant (7 km thickness), a shallow low shear velocity zone (LVZ) is centered near 20 km depth, and the sedimentary and lithospheric thicknesses both increase with age. The age-dependence of the mantle V_s model differs from a half-space conductively cooling model, implying non-conductive cooling processes. The shallow LVZ is consistent with a dry depleted mantle with a small, retained partial melt fraction of about 1% which does not extend to ages past ~1 Ma.

Keywords: ambient noise, seismic inversion, mid-oceanic ridge, lithospheric age, surface waves, lithospheric structure, low-velocity zone, partial melt, Juan de Fuca plate

1. Introduction

Seismic information on the early evolution of the oceanic mantle lithosphere near spreading ridges has been derived principally from the MELT and GLIMPSE experiments [e.g., MELT Seismic Team, 1998; Harmon et al., 2009; Yao et al., 2011] near the East Pacific Rise (EPR), a fast spreading ridge with a full spreading rate of about 14 cm/yr. The recent deployment of ocean bottom seismographs (OBS) by the Cascadia Initiative on the Juan de Fuca Plate and the open availability of these data provide the opportunity to characterize the mantle lithosphere near a slower spreading ridge (~6 cm/yr) and ultimately to extend analyses to the entire plate. Harmon et al. [2007] and Yao et al. [2011] showed that short period Rayleigh waves and the first higher mode can be observed using cross-correlations of ambient noise recorded on OBS installed near the EPR. They used these waves to constrain shear wave speeds in the oceanic crust and uppermost mantle. Here, we analyze cross-correlations of the first six-months of ambient noise recorded by OBS installed near the Juan de Fuca ridge in order to determine shear wave speeds in the crust and uppermost mantle in the young Juan de Fuca plate to an age of about 3.5 Ma (i.e., to distances up to about 100 km from the ridge crest).

Our goal is to reveal the age dependent structure of the shallow oceanic lithosphere in the young Juan de Fuca plate in order to illuminate the physical processes at work in the shallow lithosphere. In particular, we are interested in modeling the accumulation of sediments and the variation of mantle shear wave speeds in the uppermost mantle to a depth of about 60 km. Like Harmon et al. [2009] near the EPR, we compare the estimated mantle shear wave speeds with those predicted from a conductively cooling half-space, which provides evidence for non-conducting cooling processes (e.g., small scale convection, fluids advection, lateral heat flux). In addition, we compare with the more sophisticated physical model of Goes et al. [2012] in order to investigate whether aqueous fluids or partial melt are required. Goes et al. [2012] argue for a double low velocity zone (LVZ) with a shallow LVZ between about 20 and 50 km depth caused by dry melting and a deeper LVZ between about 60 and 150 km caused by solid-state anelasticity. Our model extends only to 60 km and provides no information about a deeper LVZ. Above 60 km near the Juan de Fuca ridge, however, our model is consistent

with their predictions for a LVZ produced in dry depleted mantle with a small fraction of retained partial melt (<1%).

2. Methods

2.1 Data Processing

The Cascadia Initiative (CI) experiment provides the OBS data for this study. Because a timing error was discovered by the CI team that affects some of the 50 sps data, we used only the long period 1sps channels. This restricts our analysis to 22 stations. Stations G03A, G30A and J06A are outside of our study area and are, therefore, not used and the vertical channel of station J48A failed during the deployment and is also discarded.

Figure 1 shows the study area and the 18 stations we used, 15 of which are located to the east of the Juan de Fuca ridge and provide path coverage up to about 200 kilometers into the Juan de Fuca plate. Six-months of continuous data are available for most of these stations. When we downloaded the data, horizontal components had not yet been rotated into the east-west and north-south directions, and consequently we do not use these data and restrict our analysis to vertical components (and therefore Rayleigh waves).

We computed ambient noise cross-correlations between the vertical components of all stations by applying traditional ambient noise data processing (time domain normalization, frequency domain normalization) to produce the empirical Green's functions [Bensen et al., 2007]. An example of an empirical Green's function between stations J47A and J29A is shown in **Figure 1b**. For OBS data, the Rayleigh waveforms are highly dispersed and display two Airy phases such that the short period phase (representative of the water – sediment waveguide) arrives far after the longer period phase (representative of the crystalline crust and uppermost mantle waveguide).

Frequency-time analysis is applied to the symmetric component (average of positive and negative correlation lags) of each cross-correlation to measure Rayleigh wave group and phase speed between periods of about 6 and 20 sec. Longer periods require longer time series lengths and may be obtainable as more data become available. An example frequency-time analysis (FTAN) diagram is presented in **Figure 1c** showing both the Rayleigh wave group and phase speed curves. Rayleigh wave group speeds range from about 1 km/s at the short period end to more than 3.6 km/s at longer periods and phase

speeds range from about 1.8 km/s to more than 3.6 km/s. At periods below 6 sec the phase and group speed curves would approach each other asymptotically, but are separate in the observed period band. Also below 6 sec period, Harmon et al. [2007] and Yao et al. [2011] made observations of the first higher mode, which we cannot observe with long period data. Paths that are mainly to the west of the ridge, dominated by the structure of the Pacific plate, may be more affected by the Cobb hotspot and seamount and are discarded. Dispersion measurements for paths shorter than three wavelengths or with a signal-to-noise ratio below about 10 are also discarded. A total of 106 inter-station paths are accepted.

The resulting path coverage is not ideal to produce Rayleigh wave group or phase speed maps using either traditional tomographic methods [e.g., Barmin et al., 2001] or eikonal tomography [Lin et al., 2009]. For this reason, we test the hypothesis that Rayleigh wave phase and group speeds are dependent predominantly on lithospheric age. At each period, we follow Harmon et al. [2009] and test a velocity-age relationship of the following form:

$$v = c_0 + c_1\sqrt{A} + c_2A, \quad (1)$$

where v represents either the observed inter-station Rayleigh wave group or phase velocity, A represents the seafloor age in Ma, and c_0 , c_1 , and c_2 are period dependent unknowns that differ for phase and group speeds.

For each measurement type (phase or group) and each period extending discretely from 6 sec to 20 sec, we estimate the set of coefficients c_0 , c_1 , and c_2 . The wave travel time along a path is given by the following path integral, which occurs over a path whose dependence on crustal age is prescribed by the lithospheric age model of Mueller et al. [1997]:

$$t_{path} = \int_{path} \frac{ds}{c_0 + c_1\sqrt{A} + c_2A}. \quad (2)$$

To determine the set of best fitting coefficients at each period, a grid search is performed to minimize the total squared misfit:

$$\sum_i \left(\frac{S_i^{path}}{t_i^{path}} - v_i^{path} \right)^2, \quad (3)$$

where S_i^{path} , t_i^{path} , and v_i^{path} are the inter-station path length, the predicted travel time for a particular choice of c_0, c_1 , and c_2 , and the observed wave speed for the i th path, respectively.

Figure 2a summarizes the resulting phase and group velocity versus lithospheric age curves at periods of 7, 8, 10, and 15 sec. At short periods, velocities decrease with age because water depth and sedimentary thickness are increasing. At longer periods, they increase with age because they become sensitive to the cooling mantle. The inter-station group and phase speeds are well fit by the simple velocity versus age relation given by equation (1). Misfit histograms at 7 and 15 sec period for phase velocity are presented in **Figure 2b,c**, with a root-mean-square (rms) misfit of about 1.8% and 0.9%, respectively, and a mean misfit less than 0.1%. These values represent a large improvement compared to an age-independent model. For example, the rms misfit using our estimated phase speed model at 0.5Ma is 11.3% and 3.5% at 7 and 15 sec period, respectively, with mean misfits of -9.7% and 3.2%. The age-dependent model delivers a variance reduction relative to phase speeds at 0.5 Ma of 97% and 94%, respectively, at periods of 7 and 15 sec. Because group velocity is a more difficult observable than phase velocity, the final misfit is higher but the variance reduction relative to 0.5 Ma is still 94% and 75%, respectively, at 7 and 15 sec period. Our phase velocity model neglects azimuthal anisotropy. However, we did estimate azimuthal anisotropy at all periods and found that the expected bias in isotropic shear wave speed is less than about 0.3% at all periods, which is well within estimated uncertainties.

In conclusion, the fit to the observations by the Rayleigh wave phase velocity versus age model presented by equation (1) is sufficient to base further interpretation exclusively on the age dependence of the group and phase velocities. Although other spatially dependent variations in phase speed exist (and are interesting in their own right), they can be ignored safely in our analysis. The final result of the data analysis is a set of age-dependent Rayleigh wave phase and group velocity curves such as those at 1 Ma and 3 Ma, which are presented in **Figure 3a**. The error bars are the one standard deviation misfit to the observations given by the estimated curves in **Figure 2a**.

2.2 Bayesian Monte Carlo Inversion

Examples of the data and uncertainties at 1 Ma and 3 Ma that are inverted for shear velocity in the crust and uppermost mantle are presented in [Figure 3a](#). In particular, we are interested in modeling the age dependence of such curves, which show the effects of water depth, sedimentary thickness, crustal thickness, and uppermost mantle shear wave speeds. The shear velocity model we produce is actually a V_{sv} model because it derives exclusively from Rayleigh waves.

At each age, the model is composed of four layers. (1) The top layer is water whose depth is averaged over the study area as a function of crustal age using a global bathymetry map [Amante and Eakins, 2009] in which V_s is set 0 km/sec and V_p is 1.45 km/sec. (2) The second layer comprises the sediments with a constant shear wave speed of 1 km/sec [Sun, 2000] but with a thickness that varies with age. (3) The igneous crust underlies the sediments and is parameterized by 4 cubic B-splines. (4) Finally, there is an uppermost mantle layer parameterized by 3 cubic B-splines to a depth of 80 km. At its base this layer is continuous with an underlying layer from the half-space cooling model described in Section 3. In the inversion, only four unknowns are age-dependent: sedimentary thickness and the top 3 cubic B-spline coefficients in the mantle. The other parameters are set to be constant over age. Igneous crustal thickness is set constant at 7 km [e.g., White et al., 1992; Carbotte et al., 2008]. Crustal V_s is fixed based on an initial inversion of the 2 Ma dispersion data. Fixing the igneous crust as a function of age is consistent with gravity and multichannel seismic data along the ridge [Marjanovic et al., 2011] at long spatial wavelengths. The V_p/V_s ratio in the igneous crust is set to be 1.76 (consistent with PREM) and is 2.0 in the sediments. An additional prior constraint is imposed that the velocity gradient (dV_s/dz) is negative directly below Moho.

Through physical dispersion, the final V_{sv} model is affected by an assumed Q model [Minster and Anderson, 1981]. We follow Harmon et al. [2009] and use a frequency dependent shear Q model:

$$Q(\omega) = A^{-1} \left(\omega \exp((E + PV) / RT) \right)^\alpha \quad (4)$$

where ω is frequency, R is the gas constant, P is pressure, T is temperature from the half-space cooling model described later, activation volume $V = 1.0 \times 10^5 \text{ m}^3$, $\alpha = 0.1$, and activation energy $E = 2.5 \times 10^5 \text{ J/mol}$. The coefficient A is set to 0.066 below 80 km depth and 0.022 above 70 km depth with a linear gradient between 70 and 80 km. At 1 sec period the result is a Q of 120 below 80 km and of about 300 above 70 km depth. The final model is presented at 1 sec period. Because our data only extend over a narrow period band (6-20 sec period), the physical dispersion correction is small and sensitivity to the parameters inserted into equation (4) is quite weak. For example, decreasing the Q value by half in the mantle only increases the estimated shear wave speed by about 0.3%, which lies well within the estimated uncertainties.

The inversion is performed using a Bayesian Monte Carlo formalism, which has been described in detail and applied systematically to EarthScope USArray data by Shen et al. [2013a,b]. An input model that defines the prior distribution is initially computed by performing an inversion with the dispersion curves for 2 Ma crust in which we allow the coefficients of the crustal B-splines to vary. The crystalline crust for all ages is fixed at the result of this inversion. The forward problem is computed using the code of Herrmann [<http://www.eas.slu.edu/eqc/eqccps.html>]. The best fitting model (M_0) is then used to construct the model space for the age-dependent inversion. The model space defining the prior distribution at each age is generated as follows. The sedimentary layer thickness is allowed to vary $\pm 100\%$ relative to M_0 . The top first, second and third cubic B-splines in the mantle are allowed to vary by $\pm 4\%$, $\pm 2\%$ and $\pm 1\%$, respectively, relative to M_0 , which acts to squeeze heterogeneity towards shallow depth. After this inversion, the mean and standard deviation of the posterior distribution at each age are computed at each depth. We then re-perform the inversion based on this initial mean age-dependent model, which helps to calibrate the posterior distribution.

We estimate 1-D V_{sv} models for the dispersion curves at crustal ages of 0.5, 1.0, 1.5, 2.0, 2.5, 3.0 and 3.5 Ma. The major products are an age-independent igneous crust with a thickness of 7 km, a constant V_s sedimentary layer with age-variable thickness, and age-dependent V_{sv} as a function of depth in the uppermost mantle. Water depth and sedimentary thickness as a function of age are presented in **Figure 3b**. Sediments are estimated to increase in thickness from about 100 m at 0.5 Ma to about 400 m at 3.5 Ma,

and the depth to the top of the igneous crust increases approximately linearly with age by about 500 m between 0.5 Ma and 3.5 Ma. This is consistent with results from multichannel seismic (MCS) data [Carbotte et al., 2008]. The age-independent igneous crustal model is presented in [Figure 3c](#). The mantle age-dependent shear velocity profiles appear in [Figure 3d](#). Shear wave speeds increase with age monotonically and converge by about 60 km depth below which we have little resolution. Age-dependent posterior distributions at depths of 20 km and 40 km ([Fig. 3e, f](#)) illustrate model uncertainty and show the separation of the ensemble of accepted models at different ages. The posterior distributions reflect both prior information and the Rayleigh wave phase velocity data, however, and their narrowness in part reflects the tight constraints provided by the prior information. Still, the final age-dependent model fits the data very well, as [Figure 3a](#) illustrates. The introduction of other variables in the inversion is not justified by the need to fit the data.

A low velocity zone between 15 and 40 km depth is most pronounced at young ages. At the youngest age (0.5 Ma) in our study, the minimum V_{sv} reaches ~ 4.08 km/sec at 20 km depth. With uncertainties defined as the standard deviation of the posterior distribution at each depth (e.g., [Fig. 3e, f](#)), at 20 km depth V_{sv} increases from 4.08 ± 0.02 km/sec at 0.5 Ma to 4.37 ± 0.02 km/sec at 3 Ma. At 40 km depth, V_{sv} increases from 4.16 ± 0.01 km/sec at 0.5 Ma to 4.29 ± 0.01 km/sec at 3 Ma. At greater depths both the age variation and uncertainties decrease because prior constraints strengthen. Although we possess few observations near the ridge crest, we also estimate a 0 Ma (i.e., ridge) model by extrapolating the observations back in time to 0 Ma. This model is presented as the dashed line in [Figure 3d](#), and possesses minimum V_{sv} below 4 km/s at about 20 km.

3. Discussion and Conclusions

The age-dependent mantle V_{sv} model is summarized in [Figure 4a](#), which also presents the distance to the Juan de Fuca ridge (converted from age by using a half spreading rate of ~ 30 km/Ma; Wilson, 1993). The 2-D plot is contoured with solid or dashed lines every 0.05 km/sec with solid lines at shear wave speeds of 4.2, 4.3, 4.4, and 4.5 km/s and dashed lines at 4.15, 4.25, 4.35, and 4.45 km/s. This model is compared

with shear velocities converted from a thermal half-space conductively cooling model (HSCM), which is presented in [Figure 4b](#). In constructing the HSCM, we again follow Harmon et al. [2009] and use a mantle potential temperature of 1350 °C, a thermal diffusivity of $8 \times 10^{-7} \text{ m}^2/\text{s}$, and then convert it to anharmonic Vs using the approximation of Stixrude and Lithgow-Bertelloni [2005]. The principal difference is that we apply the physical dispersion correction and convert Vs from the HSCM to 1 sec period to match the observed model. The predicted shear wave speed from the HSCM is isotropic Vs, whereas the model inferred from Rayleigh wave dispersion is Vsv. Knowledge of radial anisotropy in the upper mantle would allow for a correction between these values, but without Love waves we do not even know the relative sizes of Vsv and Vsh. However, $|V_{sv}-V_{sh}|$ is probably less than 3% [Ekstrom and Dziewonski, 1998], and may be much smaller [e.g., Dunn and Forsyth, 2003, Harmon et al., 2009] in the shallow mantle near a ridge, so the effect on Vs is almost certainly within $\pm 1\%$ assuming a Voigt-average of Vsv and Vsh. If this value were constant across the study region and we were to use it to convert the estimated Vsv to Vs in [Figure 4a](#), the transformation would shift the mean at each depth but not the variation with age. Thus, the estimated age variation is robust relative to the introduction of radial anisotropy into the model.

As observed in [Figure 4a,b](#), both the estimated model and the HSCM model possess a monotonically increasing high velocity lid at shallow mantle depths, and both have similar average shear wave speeds in the upper mantle of $\sim 4.25 \text{ km/sec}$. There are also prominent differences between them. (1) First, the fast lid is observed to thicken at a much faster rate than for the HSCM. If we define the base of the lid (or the base of the lithosphere) to be at 4.3 km/s, then by about 3 Ma ($\sim 100 \text{ km}$ from the ridge) the estimated lid thickens to $\sim 40 \text{ km}$ but the lid in the HSCM only penetrates to $\sim 25 \text{ km}$ depth. Although the choice of 4.3 km/s is ad-hoc, the observed lithospheric lid is probably more than 1.5 times thicker than predicted by the HSCM. The faster development of the lithospheric lid than predicted by the HSCM implies non-conductive cooling processes, such as lateral heat flux, small-scale convection or the vertical advection of fluids at work for the lithospheric ages we consider.

(2) A second major difference is that the estimated model possesses a prominent low velocity zone (LVZ) in the uppermost mantle (15-40 km) at young ages near the ridge

(age < 1.5 Ma), but such low wave speeds are not present in the HSCM. Low shear velocities in the mantle (<4.1 km/sec) at 15-40 km beneath the ridge also have been seen beneath the East Pacific Rise [Dunn and Forsyth, 2003; Yao et al., 2011], which was attributed to partial melt beneath the ridge. Goes et al. [2012] show that if the upper mantle is depleted in basalt, resulting in a harzburgite composition of the residue, but retains water, then V_s would be far lower than what we observe in the uppermost mantle near the Juan de Fuca ridge. However, with a dry depleted mantle devoid of partial melt, no LVZ appears and V_s is faster than we observe, as can be seen in [Figure 4c](#). To produce a shallow LVZ with V_s values similar to what we observe they have included a small retained partial melt fraction of 1%. Their values of V_s minimize at about 3.8 km/s, which is considerably slower than what we observe. However, they take their partial derivatives of anharmonic V_s relative to melt fraction from the highest values of Hammond and Humphreys [2000] and, therefore, may have over-predicted the effect of partial melt on V_s . The amplitude of the LVZ is observed to diminish with age, which is consistent with cooling and the reduction in the melt fraction. By 1.5 Ma, the velocity minimum at about 20 km has largely disappeared, which, following the interpretation presented here, would probably mean that partial melt is unlikely past about 1 Ma (i.e., 30 km from the ridge crest).

Acknowledgments The authors thank the Cascadia Initiative Expedition Team for acquiring the Amphibious Array Ocean Bottom Seismograph data and appreciate the open data policy that made the data available shortly after they were acquired. The facilities of the IRIS Data Management System were used to access some of the data used in this study. The IRIS DMS is funded through the US National Science Foundation under Cooperative Agreement EAR-0552316.

References

- Amante, C. and B. W. Eakins (2009), ETOPO1 1 Arc-Minute Global Relief Model: Procedures, Data Sources and Analysis. NOAA Technical Memorandum NESDIS NGDC-24, 19 pp.
- Barmin, M. P., M. H. Ritzwoller, and A. L. Levshin (2001), A fast and reliable method for surface wave tomography, *Pure and Applied Geophysics*, 158(8), 1351–1375, doi:10.1007/PL00001225.
- Bensen, G.D., M.H. Ritzwoller, M.P. Barmin, A.L. Levshin, F. Lin, M.P. Moschetti, N.M. Shapiro, and Y. Yang, Processing seismic ambient noise data to obtain reliable broad-band surface wave dispersion measurements, *Geophys. J. Int.*, 169, 1239-1260, doi: 10.1111/j.1365-246X.2007.03374.x, 2007.
- Carbotte, S. M., M. R. Nedimović, J. P. Canales, G. M. Kent, A. J. Harding, and M. Marjanović (2008), Variable crustal structure along the Juan de Fuca Ridge: Influence of on-axis hot spots and absolute plate motions, *Geochem. Geophys. Geosyst.*, 9, Q08001, doi:10.1029/2007GC001922.
- Dunn, R. A., and D. W. Forsyth (2003), Imaging the transition between the region of mantle melt generation and the crustal magma chamber beneath the southern East Pacific Rise with short-period Love waves, *J. Geophys. Res.*, 108(B7), 2352, doi:10.1029/2002JB002217.
- MELT Seismic Team, The (1998), Imaging the deep seismic structure beneath a mid-ocean ridge: The MELT experiment, *Science*, 280, 1215–1218, doi:10.1126/science.280.5367.1215.
- Goes, S., J. Armitrage, N. Harmon, H. Smith, and R. Huisman (2012), Low seismic velocities below mid-ocean ridges: Attenuation versus melt retention, *J. Geophys. Res.*, 117, B12403, doi:10.1029/2012JB009637.
- Hammond, W. C., and E. D. Humphreys (2000), Upper mantle seismic wave velocity: Effects of realistic partial melt geometries, *J. Geophys. Res.*, 105, 10,975–10,986
- Harmon, N., D. Forsyth, and S. Webb (2007), Using Ambient Seismic Noise to Determine Short-Period Phase Velocities and Shallow Shear Velocities in Young Oceanic Lithosphere, *Bulletin of the Seismological Society of America*, 97(6), 2009–2023, doi:10.1785/0120070050.
- Harmon, N., D. W. Forsyth, and D. S. Weeraratne (2009), Thickening of young Pacific lithosphere from high-resolution Rayleigh wave tomography: A test of the conductive cooling model, *Earth and Planetary Science Letters*, 278, 96–106, doi:10.1016/j.epsl.2008.11.025.
- Lin, F.-C., M. H. Ritzwoller, and R. Snieder (2009), Eikonal tomography: surface wave tomography by phase front tracking across a regional broad-band seismic array, *Geophysical Journal International*, 177(3), 1091–1110, doi:10.1111/j.1365-246X.2009.04105.x.

- Marjanović, M., S. M. Carbotte, M. R. Nedimović, and J. P. Canales (2011), Gravity and seismic study of crustal structure along the Juan de Fuca Ridge axis and across pseudofaults on the ridge flanks, *Geochem. Geophys. Geosyst.*, 12, Q05008, doi:10.1029/2010GC003439.
- Minster, J.B. and D.L. Anderson (1981), A model of dislocation-controlled rheology for the mantle, *Phil. Trans. R. Soc. London*, 299, 319-356.
- Mueller, R. D., W. R. Roest, J.-Y. Royer, L. M. Gahagan, and J. G. Sclater (1997), Digital isochrons of the world's ocean floor, *J. Geophys. Res.*, 102, 3211–3214.
- Shen, W., M.H. Ritzwoller, V. Schulte-Pelkum, F.-C. Lin, Joint inversion of surface wave dispersion and receiver functions: A Bayesian Monte-Carlo approach, *Geophys. J. Int.*, 192, 807-836, doi:10.1093/gji/ggs050, 2013.
- Shen, W., M.H. Ritzwoller, and V. Schulte-Pelkum, A 3-D model of the crust and uppermost mantle beneath the central and western US by joint inversion of receiver functions and surface wave dispersion, *J. Geophys. Res.*, doi:10.1029/2012JB009602, 118, 1-15, 2013.
- Stixrude, L., and C. Lithgow-Bertelloni (2005), Mineralogy and elasticity of the oceanic upper mantle: Origin of the low-velocity zone, *J. Geophys. Res.*, 110, B03204, doi:10.1029/2004JB002965.
- Sun, Y.F., 2000, Core-log-seismic integration in hemipelagic marine sediments on the eastern flank of the Juan de Fuca Ridge, in Fisher, A., Davis, E., and Escutia, C. (Eds.), ODP Scientific Results, 168, 21-35.
- White, R. S., D. McKenzie, and R. K. O'Nions (1992), Oceanic crustal thickness from seismic measurements and rare earth element inversions, *J. Geophys. Res.*, 97(B13), 19683–19715, doi:10.1029/92JB01749.
- Wilson, D. S. (1993), Confidence intervals for motion and deformation of the Juan de Fuca Plate, *J. Geophys. Res.*, 98(B9), 16053–16071, doi:10.1029/93JB01227.
- Yao, H., P. Gouédard, J. A. Collins, J. J. McGuire, and R. D. van der Hilst (2011), Structure of young East Pacific Rise lithosphere from ambient noise correlation analysis of fundamental- and higher-mode Scholte-Rayleigh waves, *Comptes Rendus Geoscience*, 343(8–9), 571–583, doi:10.1016/j.crte.2011.04.004.

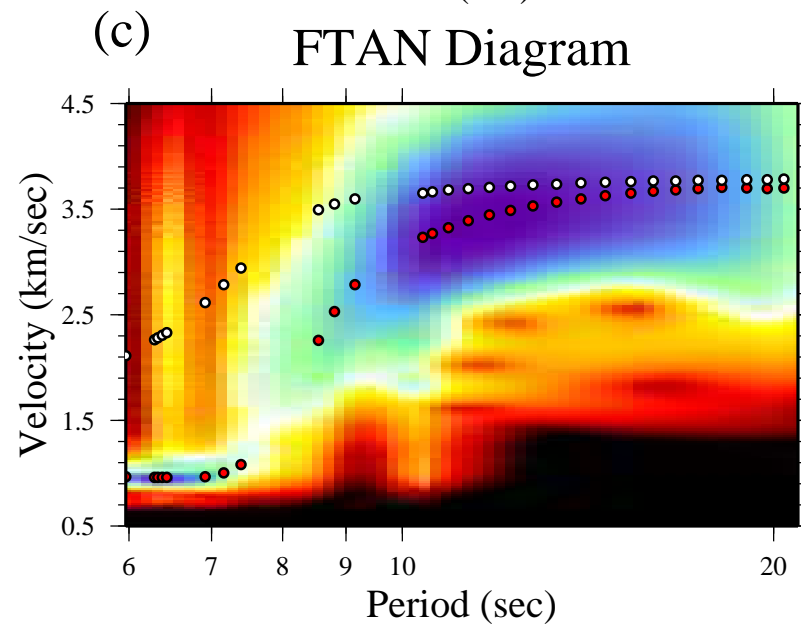
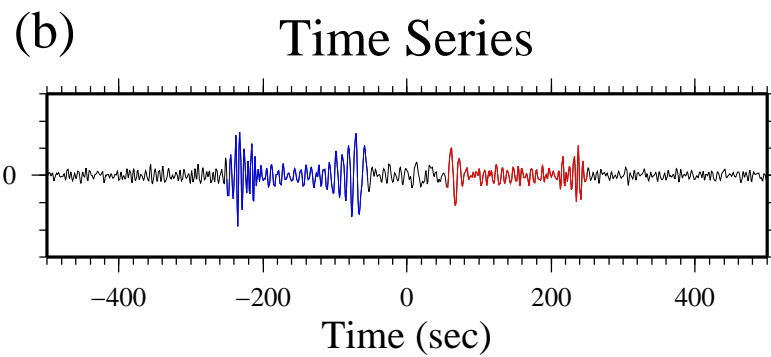
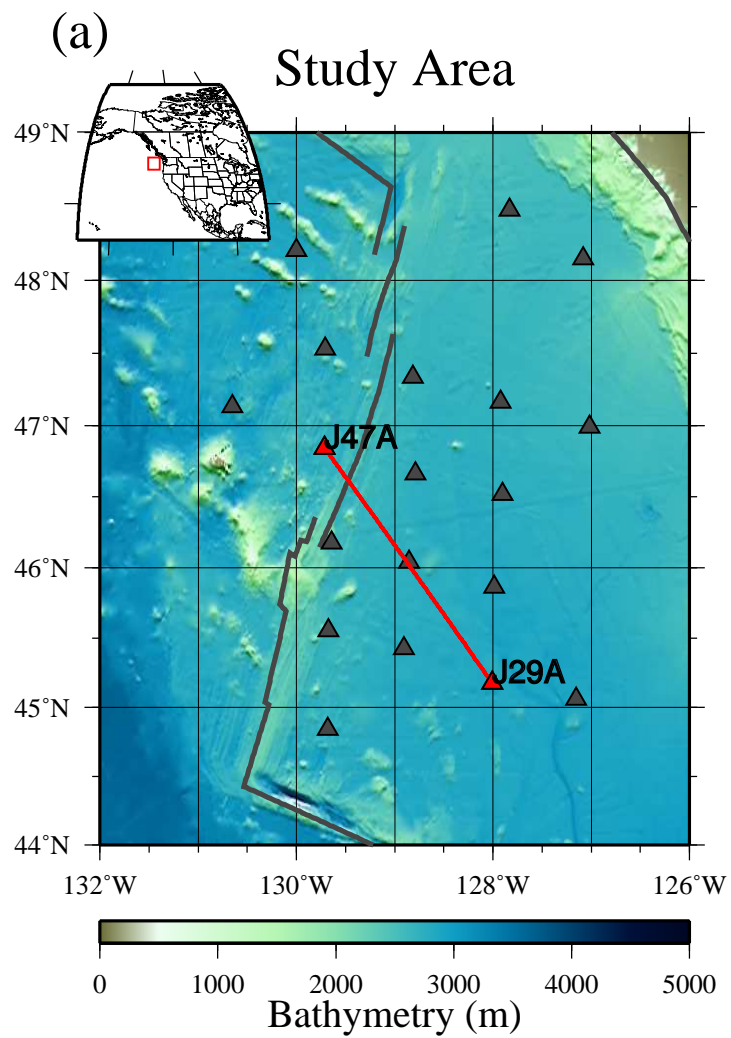
Figure Captions

Figure 1. (a) Location of the 18 long period Cascadia Initiative OBS stations used in this study (triangles). Stations J29A and J47A are marked red. Gray lines indicate the mid-ocean ridge. (b) Example 6 month cross-correlation between data from stations J29A and J47A. The waveform is colored red or blue for the positive or negative correlation lag with group speeds ranging between 0.9 and 4.15 km/sec. (c) Rayleigh wave velocity versus period (FTAN) diagram of the symmetric component of the signal shown in (b). Background color indicates the spectral amplitude and group and phase speeds are shown with red and white circles, respectively.

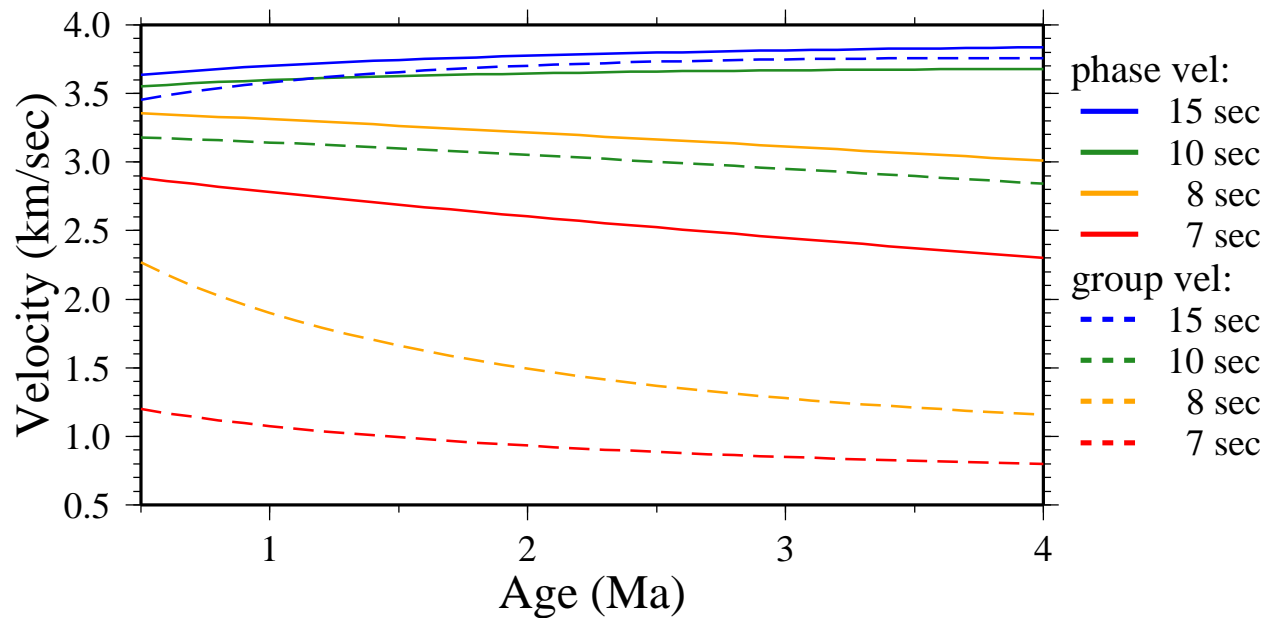
Figure 2. (a) The estimated age-dependent Rayleigh wave phase (solid lines) and group (dashed lines) velocities at 7 (red), 8 (orange), 10 (green) and 15 (blue) sec period as a function of lithospheric age. (b) – (c) Histograms of misfit to the observed inter-station phase velocities at 7 and 15 sec periods produced by the estimated age-dependent curves (blue histograms) and an age-independent model at 0.5 Ma (white histograms). The mean and standard deviation of misfit are shown for the age-dependent model and the model at 0.5 Ma. The variance reduction is presented for the age-dependent model from relative to the 0.5 Ma model.

Figure 3. (a) Estimated dispersion curves for seafloor ages of 1 Ma (red) and 3 Ma (black). Error bars show the velocity and estimated uncertainty. Solid curves are the predictions from the inverted age-dependent shear velocity model. (b) Water depth (blue line), estimated sedimentary layer thickness (red line), and the depth of crystalline basement below ocean surface (grey line), which is the sum of water depth and sedimentary layer thickness. (c) Estimated crustal V_s model, which varies in age only by sediment thickness and water depth. (d) The estimated age-dependent shear-wave velocity models (V_{sv}) in the mantle from 0.5 to 3 Ma. The model extrapolated to 0 Ma is shown with the dashed line. All models are presented at 1 sec period. (e) The posterior distribution of V_{sv} models for each seafloor age at 20 km depth: 0.5 Ma (red), 1 Ma (orange), 2 Ma (green), 3 Ma (blue). (f) Same as in (e), but for 40 km depth.

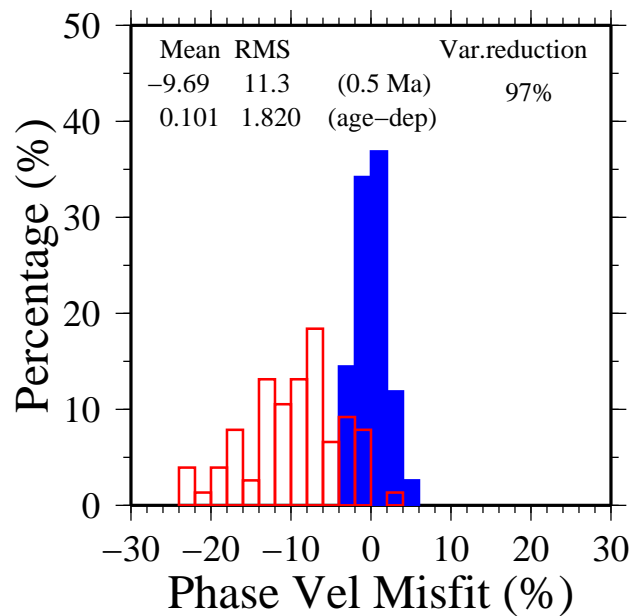
Figure 4. Comparison of (a) the estimated V_{sv} model and (b) a half-space conductive cooling model (HSCM) as a function of seafloor age. V_{sv} values in increments of 0.1 km/sec are contoured with solid lines and values in odd multiples of 0.05 km/sec are contoured with dashed lines. (c) Comparison of our extrapolated 0 Ma model (dashed line) in the mantle compared with two models from Goes et al. (2012): (blue) dry depleted mantle with no melt and (red) dry depleted mantle with 1% retained melt fraction. Our model has been converted to 50 sec period to compare with the results of Goes et al. (2012) and, therefore, differs somewhat from the result in Fig. 3d.



(a) Velocity–Age Relationships



(b) Misfit 7.0 sec



(c) Misfit 15.0 sec

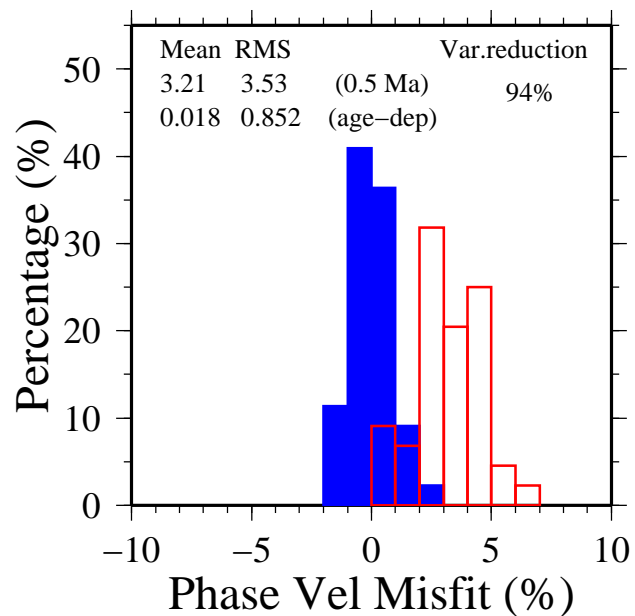


Fig 3.

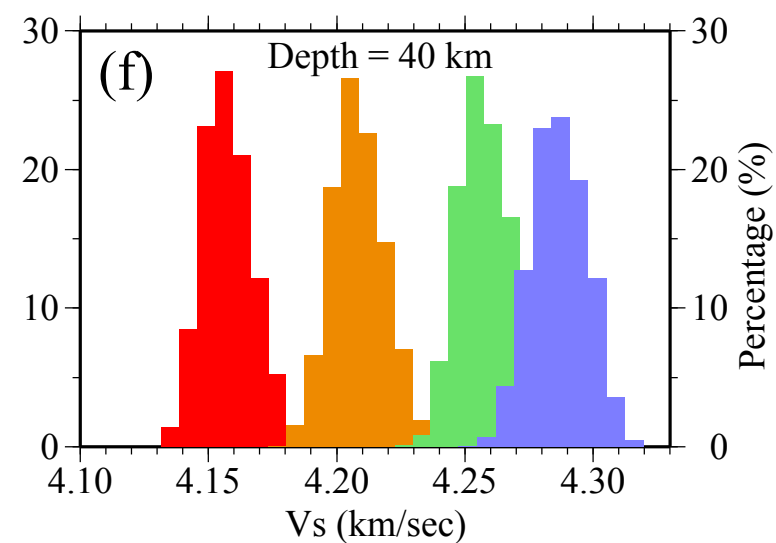
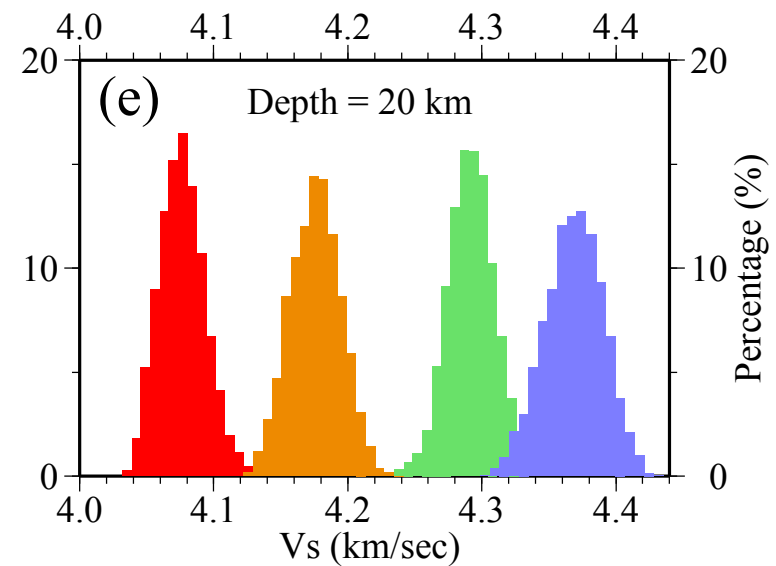
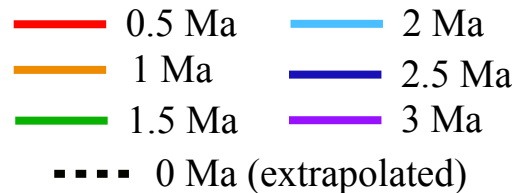
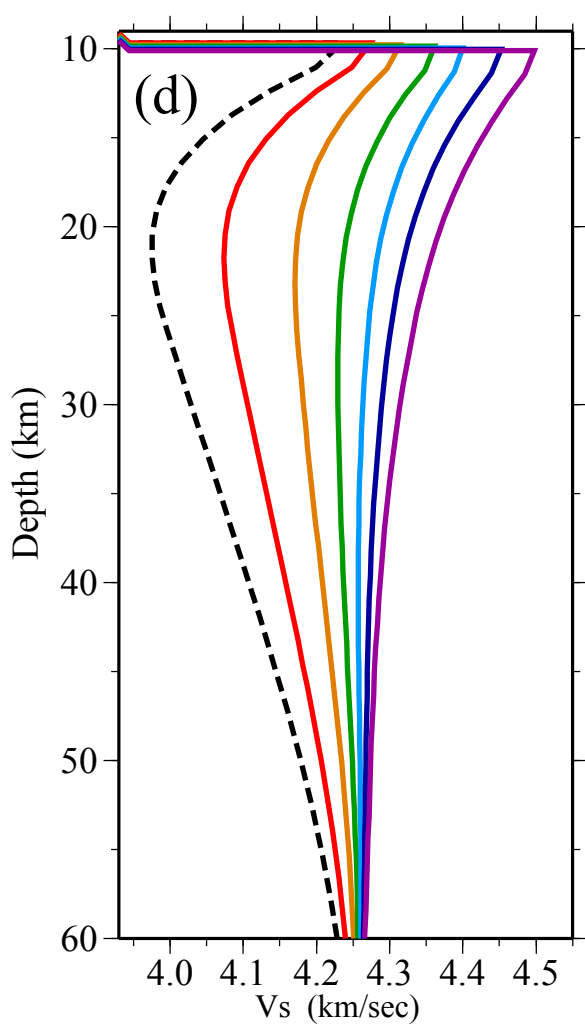
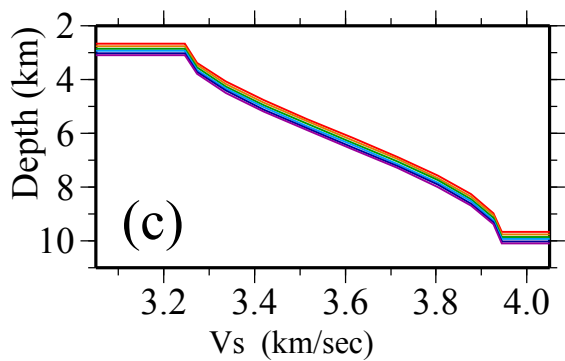
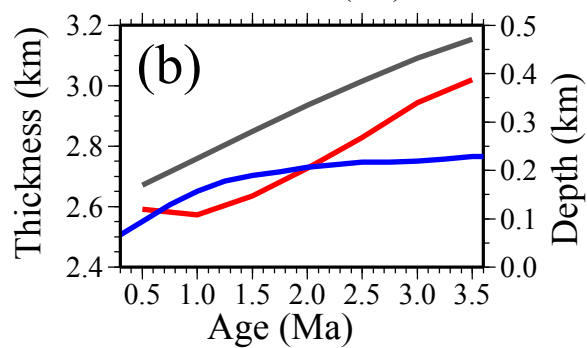
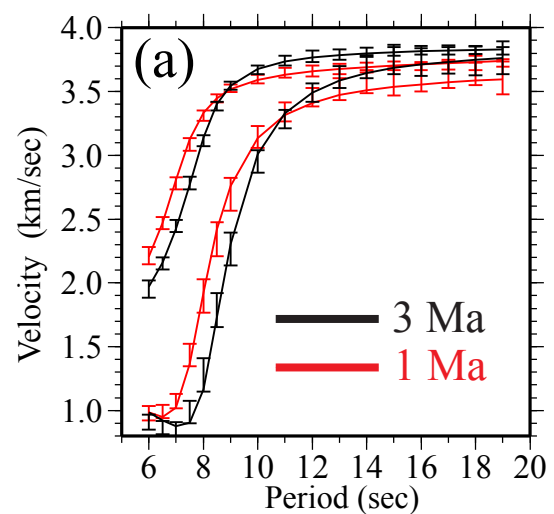


Figure 4.

